

Qualitative Theory for Lensed QSOs

Prasenjit Saha

*Astronomy Unit, School of Mathematical Sciences
Queen Mary and Westfield College
University of London
London E1 4NS, UK*

and

Liliya L.R. Williams

*Department of Physics and Astronomy
University of Minnesota
116 Church Street SE
Minneapolis, MN 55455*

ABSTRACT

We show that some characteristics of multiply-imaged QSO systems are very model-independent and can be deduced accurately by simply scrutinizing the relative positions of images and galaxy-lens center. These include the time-ordering of the images, the orientation of the lens potential, and the rough morphology of any ring. Other features can differ considerably between specific models; H_0 is an example. Surprisingly, properties inherited from a circularly symmetric lens system are model-dependent, whereas features that arise from the breaking of circular symmetry are model-independent. We first develop these results from some abstract geometrical ideas, then illustrate them for some well-known systems (the quads Q2237+030, H1413+117, HST14113+5211, PG1115+080, MG0414+0534, B1608+656, B1422+231, and RXJ0911+0551, and the ten-image system B1933+507), and finally remark on two systems (B1359+154 and PMN J0134-0931) where the lens properties are more complex. We also introduce a Java applet which produces simple lens systems, and helps further illustrate the concepts.

Subject headings: gravitational lensing

1. Introduction

Multiply-imaged QSOs are studied in pursuit of a variety of goals. The positions and relative magnifications of the images reveal something about the mass distribution of lensing galaxies, and

if microlensing is observable then they also probe the mass function on stellar scales. If time delays are measurable they supply estimates of the Hubble constant H_0 , and image statistics over many different lenses indicate something about the dimensionless global cosmological parameters, Ω and Λ . Microlensing also constrains the intrinsic sizes of the sources, and possibly the bulk velocity or velocity dispersion of the galaxy. Finally, individual images in a multiple-image system provide nearby but distinct lines of sight through the intergalactic medium. These are discussed at length in recent reviews (Wambsganss 1998; Claeskens & Surdej 2002; Courbin et al. 2003) and older but still relevant works (Wambsganss 1990; Schneider, Ehlers, & Falco 1992; Blandford & Narayan 1992; Narayan 1998).

With so much interest, it is not surprising that many models of galaxy lenses have been developed, employing several different methods. What is somewhat surprising, however, is that some features of individual lenses are robustly model-independent while others are very model-dependent. We defer detailed references until the section on case studies, but for now we remark that different models of any given system always seem to agree about four aspects:

1. the time-ordering of the images, i.e., the ordering of time delays if the source is variable (but not the *values* of the time delays);
2. the direction of the source’s displacement, relative to the lens center;
3. the orientation of the lens-potential’s ellipticity, if significant; such ellipticity often indicates external shear from other galaxies;
4. the rough morphology of an Einstein ring, which can be predicted from QSO images alone.

At the same time, a much sought-after quantity:

0. the projected radial density profile, which decides the mass normalization and the conversion between time delays and H_0 ,

is highly model-dependent.

Since the points 1–4 are model-independent, one may wonder if they can be understood in a model-independent way. In this paper we show that indeed they can, using some abstract but basically geometrical ideas. The key concepts were introduced by Blandford & Narayan (1986), who really initiated the qualitative theory of lensing. Other aspects of this paper were anticipated by Blandford & Kovner (1988), and Wucknitz (2002).

2. Some invisible curves

Like many areas of physics, gravitational lensing can be elegantly approached through a variational principle, Fermat’s principle, which has been formulated for gravitational lensing through

several routes (Schneider 1985; Blandford & Narayan 1986; Kovner 1990; Nityananda & Samuel 1992). Of particular interest is the arrival-time surface $\tau(\vec{\theta})$, which is the light-travel time (in suitable units) for a virtual photon arriving from sky-position $\vec{\theta}$, visualized as a surface. According to Fermat’s principle, real photons come from $\vec{\theta}$ for which $\tau(\vec{\theta})$ is stationary; that is, images form where the arrival-time surface has a maximum, minimum, or saddle point.

The arrival-time surface is a function of the unlensed sky-position $\vec{\beta}$ and the sky-projected density (again, in suitable units) $\kappa(\vec{\theta})$. A concise expression for the arrival time is

$$\tau(\vec{\theta}) = \frac{1}{2}(\vec{\theta} - \vec{\beta})^2 - 2\nabla^{-2}\kappa(\vec{\theta}). \quad (1)$$

The first term in Equation (1) is geometrical, while the second term is the gravitational time delay due to the lens, also called the lens potential and written as $\psi(\vec{\theta})$. The unusual symbol ∇^{-2} is just an inverse Laplacian operator; it denotes the operation of solving Poisson’s equation (in two dimensions).

For calculations it is conventional to use units such that κ is dimensionless and of order unity while τ is also dimensionless and measured in arcsec^2 . But the arrival-time $t(\vec{\theta})$ and surface $\Sigma(\vec{\theta})$ in physical units are easily recovered through the relations

$$t(\vec{\theta}) = T_0 \times \tau(\vec{\theta}), \quad \Sigma(\vec{\theta}) = \Sigma_0 \times \kappa(\vec{\theta}), \quad (2)$$

$$T_0 = h^{-1} \frac{(1 + z_L) D_L D_S}{c D_{LS}} \simeq z_L \times 100 h^{-1} \text{ days arcsec}^{-2}, \quad (3)$$

$$\Sigma_0 = \frac{c^3}{4\pi G} \frac{T_0}{(1 + z_L)} \simeq z_L \times 10^{11} h^{-1} M_\odot \text{ arcsec}^{-2}. \quad (4)$$

There is really only one scale in the problem: T_0 , which is of order the Hubble time; the density scale Σ_0 (known as the critical density) is essentially equivalent.

The derivatives of the arrival time are very important. The condition for an image at $\vec{\theta} = \vec{\theta}_{\text{im}}$, being that the arrival time has a maximum, minimum, or saddle point at $\vec{\theta}_{\text{im}}$, is

$$\nabla\tau(\vec{\theta}_{\text{im}}) = 0. \quad (5)$$

Equation (5) defines a mapping from $\vec{\theta}_{\text{im}}$ to $\vec{\beta}$, which is the lens equation. Further, $\nabla\nabla\tau(\vec{\theta}_{\text{im}})$ is the inverse (tensor) magnification of the image.

Elsewhere we have developed modeling techniques that concentrate on reconstructing the arrival-time surface. At first we thought of discretizing τ (Williams & Saha 1995) but later concluded (Saha & Williams 1997) that discretizing κ is a better idea. In the present paper we are interested not in model-making as such, but in gaining intuition for the shape of the arrival-time surface, the locations of images, and how the two relate to each other. For this purpose, it is useful to introduce some abstract (and hence invisible) curves.

2.1. Saddle point contours

Saddle-point contours are special contours in the arrival-time surface: contours that pass through saddle points, or equivalently, self-crossing contours, as first discussed in connection with gravitational lensing by Blandford & Narayan (1986). Their usefulness is that they form a sort of skeleton for a multiple-image system, as we now explain.

In the absence of lensing $\tau(\vec{\theta})$ is a parabola, all the contours are circular, and the sole image is at the minimum $\vec{\theta} = \vec{\beta}$. For a small lensing mass, the shape changes slightly from being a parabola and the minimum moves a little. For large enough mass, a qualitative change occurs, in that a contour becomes self-crossing. There are two ways in which a self-crossing can develop: as a kink on the outside of a contour line (a figure ‘8’, called a lemniscate), or a kink on the inside (called a limaçon). These are illustrated in Figure 1. With the original contour having enclosed a minimum, a lemniscate produces another minimum, plus a saddle-point at the self-crossing, while a limaçon produces a new maximum plus a saddle point. (The previous sentence remains valid if we interchange the words ‘maximum’ and ‘minimum’.) The process of contour self-crossing can then repeat around any of the new maxima and minima, producing more and more new images, but always satisfying

$$\text{maxima} + \text{minima} = \text{saddle points} + 1. \quad (6)$$

The self-crossing or saddle-point contours form a sort of skeleton for the multiple-image system. Many different configurations are possible in principle and are tabulated in Blandford & Narayan (1986), but in practice lensed quasars characteristically have one of two configurations: double quasars have a limaçon, while quads have a lemniscate inside a limaçon, as in the rightmost part of Figure 1. A limaçon is needed to produce a maximum (marked ‘ H ’ in the Figure 1) which will be located at the center of the lensing galaxy. Since galaxies tend to have sharply-peaked central densities, the corresponding image is highly demagnified and (so far) always unobservable.¹ Thus lensed quasars are doubles or quads: an incipient third or fifth image hides at the center of the lensing galaxy.²

2.2. Critical curves and caustics

Critical curves and caustics were introduced into gravitational lensing by Bourassa & Kantowski (1975), and later explored more fully by Blandford & Narayan (1986).

¹However, a central image is seen in some clusters, notably in Cl0024+1654 (see, for example, Astronomy Picture of the Day, <http://antwrp.gsfc.nasa.gov/apod/ap980614.html>).

²In cluster lenses, however, a single density peak does not always dominate, and other image configurations are possible. Three-image configurations involving an isolated lemniscate are common, and a limaçon with the maximum observable is also possible. See AbdelSalam et al. (1998) for examples in Abell 370.

They involve derivatives of the arrival time, and thus are not as intuitive as saddle-point contours. But they are perhaps better known.

Critical curves are curves on the image plane where the magnification is infinite. More formally, they are curves where $\nabla\nabla\tau(\vec{\theta})$ has a zero eigenvalue. Clearly, at minima of τ both eigenvalues of $\nabla\nabla\tau$ will be positive, at maxima both eigenvalues will be negative, and at saddle points one eigenvalue will be positive and one negative. Thus critical curves separate regions of the image plane that allow minima, saddle points, and maxima.

Mapping critical curves from the $\vec{\theta}$ to $\vec{\beta}$ via the lens equation (5) gives caustic curves. Caustics separate regions on the source plane that give rise to different numbers of images.

In non-astronomical optics, caustics are curves not on the source plane but on the ‘observer plane’. For example, the patterns at the bottom of a swimming pool are caustics. In fact, caustics can be defined both on the source plane and the observer plane—after all, light rays can run forwards or backwards. In gravitational lensing we are more interested in caustics on the source plane because we are (usually) concerned with one observer on the ground and many sources on the sky, whereas with a swimming pool the reverse applies.

2.3. Apparent-shear ellipse

The apparent-shear ellipse is the minimum-area ellipse passing through the four images of a quad. Being specific to quads, the apparent-shear ellipse does not have the same deep significance as the other invisible curves, but is still very interesting. It was introduced by Wucknitz (2002) on the basis of models. Here we will motivate it in a model-independent way.

The geometrical part of the arrival time in equation (1) is constant on circles. The mass distributions $\kappa(\vec{\theta})$ of galaxies do have significant ellipticity, but ∇^{-2} tends to suppress the ellipticity in the potential. As a result, the images in a quad produced by a galaxy potential will be roughly in circles centered at $\vec{\beta}$. The situation changes if other group galaxies or a cluster make a large contribution to the potential, because then the potential can become more elliptical. In particular, consider a constant external shear, given by a potential $\frac{1}{2}\gamma_1(\theta_x^2 - \theta_y^2) + \gamma_2\theta_x\theta_y$. The arrival-time will be

$$\tau(\vec{\theta}) = \frac{1}{2}(\vec{\theta} - \vec{\beta})^2 + \frac{1}{2}\gamma_1(\theta_x^2 - \theta_y^2) + \gamma_2\theta_x\theta_y - 2\nabla^{-2}\kappa_{\text{galaxy}}(\vec{\theta}). \quad (7)$$

Here the geometrical plus shear terms taken together behave like a single geometrical term that is constant on ellipses of eccentricity $\gamma = \sqrt{\gamma_1^2 + \gamma_2^2}$. If the galaxy potential is fairly circular the images of a quad will still lie on an eccentric ellipse.

Motivated by the above arguments, we consider ellipses

$$\frac{1}{2}(\vec{\theta} - \vec{\beta}')^2 + \frac{1}{2}\gamma'_1(\theta_x^2 - \theta_y^2) + \gamma'_2\theta_x\theta_y = c \quad (8)$$

and solve for $\beta'_x, \beta'_y, \gamma'_1, \gamma'_2, c$ such that (i) all four images of a given quad lie on the ellipse, and

(ii) $\gamma_1'^2 + \gamma_2'^2$ is minimized. (This is just a matter of numerically solving 5 simultaneous linear equations.) We call the fitted value of $\sqrt{\gamma_1'^2 + \gamma_2'^2}$ the ‘apparent shear’ or γ_{app} . (Wucknitz calls it the ‘critical shear’ because in his models it has an interesting relation to the critical density.) The apparent shear is not the actual shear $\gamma = \sqrt{\gamma_1^2 + \gamma_2^2}$, because it ignores dependence of image positions on $\kappa_{\text{galaxy}}(\vec{\theta})$. But still, we expect the apparent shear will give some indication of the direction and scale of the true shear.

3. Model-independent features

We now study the qualitative features of lensing by typical galaxy potentials: elliptical, but having a high central density. A simple example of such a potential is

$$\psi(\vec{\theta}) = (\theta_x^2 + \theta_y^2 + r_c^2)^{\frac{1}{2}} + \frac{1}{2}\gamma(\theta_x^2 - \theta_y^2) \quad (9)$$

which is a non-singular isothermal with core radius r_c plus external shear γ corresponding to external mass to the N or S. In Figures 2 to 4³ we take $r_c = 0.1$ and $\gamma = 0.2$ in the potential (9) as an illustration, and then examine what happens for different source positions, through caustics, critical curves, and saddle-point contours. Of course, the features we will discuss do not depend on the details of the potential.

The layout in Figures 2 to 4 is as follows.⁴

- The right panels show saddle-point contours and images. The central image is always a maximum, the contour self-crossings are saddle points, while the remaining images are minima of the arrival time.
- The middle panels show critical curves and images. The outer critical line is aligned with the long axis of the potential. Recall that critical lines are where an eigenvalue of the magnification changes sign. The consequence for this lens is that any image outside both critical curves is a minimum, any image between the critical curves is a saddle point, and any image inside both critical curves is a maximum, all irrespective of the source position. Image parities can be verified by comparing with the saddle-point contours.
- The left panels show caustics and source positions. (For better visibility, the caustic panels have been expanded by a factor of two relative to the other panels.) The two caustic curves demarcate regions from where a source produces 1, 3, and 5 images. The two critical lines are maps of the caustics to the image plane, but the *inner* (diamond) caustic maps to the *outer* critical line.

³Figures of this type, i.e., showing source and image positions in source and lens plane, with caustics and critical curves, respectively, were first used by Narayan & Grossman (1989) and Blandford et al. (1989).

⁴An interactive version of Figures 2 to 4, as a Java applet, is accessible via <http://ankh-morpork.maths.qmul.ac.uk/~saha/lens/>

3.1. A classification scheme for doubles and quads

Depending on the position of the source relative to the diamond caustic of an elliptical lens we can identify four kinds of quads and two kinds of doubles. We call these *core quads*, *inclined quads*, *long-axis quads*, and *short-axis quads*, *inclined doubles*, and *axial doubles*.

The top panels in Figure 2 show a core quad: the source is near the center of the diamond caustic, and the images are distributed in a cross. (We disregard the unobservable central image.) The middle panels in the figure shows an inclined quad: the source is just inside the diamond caustic and away from the cusps; two of the images (a saddle point and a minimum) are close together, with the remaining two roughly 120° on either side. The bottom panels show an inclined double: the source has moved outside the diamond caustic, and two images have merged and disappeared.

The upper panels in Figure 3 show a long-axis quad: the source is just inside a cusp in the direction of the long axis of the lens potential; one image (a saddle point) is close to the center while the other three are on the opposite side and further out. The lower panels show an axial double: the source has moved outside the diamond caustic and two images have merged and disappeared, leaving two images nearly colinear with the center of the lens.

The upper panels in Figure 4 show a short-axis quad: here the source is just inside a cusp in the direction of the short axis of the lens; three images are close to the galaxy while one (a minimum) is on the opposite side and further out. The lower panels show another axial double: again the source has moved outside the diamond caustic and two images have merged and disappeared, leaving two images nearly colinear with the center of the lens.

The four quad and two double image-morphologies are all distinct, and all the doubles and quads in the CASTLe survey (Kochanek et al. 1998) are easily classified according to morphology. But that is only the first step. We now show that even without resorting to any modeling, examination of the relative locations of the images with respect to each other and to the center of the lensing galaxy can reveal a wealth of information.

3.2. The time-ordering of images

In doubles, the image further from the galaxy center is a minimum and arrives first, while the image closer to the galaxy center is a saddle point and arrives second. We do not know if this is mathematically compulsory (intuitively we feel not). Nevertheless we know of no exceptions, either observed or in any plausible model.

For quads, time ordering is more subtle. Extrapolating from doubles, one might expect that images arrive in order of decreasing distance from the lens center—but this is not always true: the CLASS lens B1608+656 (the only quad so far to have its image-ordering observed directly) refutes this (Fassnacht et al. 1999). Nevertheless, the idea of saddle-point contours lets us reliably infer

image-ordering in nearly all cases, including B1608.

In Figure 5 we show saddle point contours in a generic quad, with images labeled by increasing arrival time. The two loops of the lemniscate enclose two minima, the larger loop containing the deeper minimum 1 and the smaller loop containing 2. Of the two saddle points, the lemniscate has 3 and the limaçon has 4. The small loop of the limaçon has the incipient fifth image, which is a maximum at the center of the galaxy. (In a double, the lemniscate is absent; 1 remains 1, while 4 becomes 2.) We can restate the above as two rules: (i) 1 and 2 are minima, while 3 and 4 are saddle points, and (ii) minima and saddle points alternate in position angle (PA). Considering isochrones on the arrival-time surface, we can formulate two more rules: (iii) being the global minimum, 1 has the greatest number of isochrones separating it from the lens center, so 1 is the furthest or nearly the furthest from the lens center, (iv) analogously 4 is the closest or nearly the closest to the lens center. Finally, examining the merging images in Figures 2 to 4 we see that (v) if two images are close together, they will be 2 and 3. After a little practice at using rules (i)–(v), the image ordering is usually obvious. In the most symmetric central quads 1 and 2 are hard to distinguish, but apart from this, first impressions and detailed modeling (and observations, where available) always give the same image order.

We suggest that labeling images by time order would be much preferable to labeling A, B, C, etc., by brightness as is usual at present. First, time order is physically motivated and unique; brightness order can change with wavelength, and also with time due to microlensing. Second, time order is closely connected to the image configuration, and thus easier to remember.

3.3. The direction of the source’s displacement

From Figures 2 to 4 it is clear that the PA of the source with respect to the center of the lensing galaxy is close to the PA of image 1, which is not surprising since the global minimum 1 is the image least changed from the unlensed case. Examining these figures further, we can see that the source does not have exactly the same PA as 1: it always leans away from 1 and towards the 2-3 pair, though by different angles. The radial displacement of the source may be very different from that of the images.

By itself, the location of a source is not very exciting. However, if a source has several components, the inferred source position reveals something of the source morphology. In Section 5 we will discuss the example of B1933+507, where three components of a jet are lensed; there are many lens models, but they all require the source components to be colinear.

3.4. The orientation of the main source of shear

In a circularly symmetric case all the images are equidistant from the center, forming an Einstein ring. When the source moves off axis, or the lens becomes moderately elongated, the images still stay approximately equidistant from the center, typically to within 20%. In fact, it is very hard to induce the images to spread over a larger radial range with one moderately elliptical lensing galaxy. So a narrow spread in images' galacto-centric distances indicates small or zero external shear and moderate galaxy ellipticity.

An external mass (such as another group galaxy) has a different and easily noticeable effect. Suppose there is an external mass to the N. It will contribute most to the arrival time in the N; we can imagine the external mass pushing up the northern part of the arrival-time surface. The effect on the stationary points will be to push the northernmost and southernmost image towards the center and the easternmost and westernmost images away from the center; there will be a large spread in galacto-centric radii among the images. We have already come to a similar conclusion via a more algebraic argument above (near Equation 7). Specifically, if there is an external mass to the N, the long axis of the lens potential will be NS, and the images will lie on an eccentric ellipse whose major axis is roughly EW.

Examining the quads in Figures 2 to 4 again we can easily find the direction of the shear to within 20–30°, just by looking at the images. Detailed modeling does not do much better than that.

3.5. The morphology of rings

Rings and partial rings in multiple-image systems are images of the QSO host galaxy. We can predict their appearance approximately, simply from the arrival-time surface of QSO source. Now, points of zero gradient on the arrival-time surface correspond to QSO images; we may hope that regions of small gradient correspond to images of the host galaxy. In fact, if the host galaxy is modeled by a conical brightness profile, where the source brightness falls off linearly with distance away from the source center until it becomes zero, then the density of isochrones on the arrival-time surface represents the inverse brightness of the rings (Saha & Williams 2001). In other words, to a first approximation, the ring will be brightest where the contours on the arrival-time surface are furthest apart.

From the above, we conclude that rings in quads will be brightest in the arc 1–2–3–4, and fainter or absent in the arc 4–1 (because arrival-time isochrones will be more closely packed in the latter region).

Similar conclusions can also be reached by a very different route, via caustics and critical curves (Blandford & Kovner 1988).

4. Model-dependent features

In the previous section we saw that multiply-imaged lenses permit a preliminary reconstruction without any modeling; in particular, points 1–4 of the Introduction can be inferred. Yet some features, in particular point 0 of the Introduction, are very difficult to constrain even with detailed modeling. What is so different about features like point 0?

Surprisingly, it turns out the properties of an image system that are shared with its circularly symmetric ‘cousin’ are very model-dependent and hard to constrain, whereas properties that *arise* because of the breaking of circular symmetry are relatively model-independent and robustly reproduced by even a rudimentary model. The second category includes points 1–4 above, while point 0 belongs to the first category. The reason can be appreciated intuitively. In a circularly symmetric system the mass of the galaxy, its radial density distribution, and the observer/lens/source distances are all degenerate; an infinite set of combinations of these parameters will give rise to exactly the same arrival time surface. When the symmetry is broken the arrival time surface acquires new features: distinct images appear, ring breaks up into pieces, etc. However, the ambiguity in the galaxy radial profile persists when the symmetry is broken.

The most important example of a degeneracy inherited from a circularly-symmetric lens is the magnification transformation (Falco et al. 1985) or the mass-disk degeneracy, which can be interpreted as stretching the arrival-time surface without moving its stationary points (Saha 2000). Mathematically, it involves multiplying $1 - \kappa$, $\vec{\beta}$, and T_0 (Eq. 3), all by the same constant, s . Physically, the degeneracy involves first rescaling the lens-mass distribution by s , and then adding a mass sheet of surface mass density $1 - s$, expressed in terms of critical density for lensing. Rescaling $1 - \kappa$ changes the radial density slope of the new mass distribution (galaxy+mass sheet), rescaling $\vec{\beta}$ changes all the magnifications in step (while keeping the relative magnifications fixed), and rescaling T_0 changes the inferred h from the same data. The image plane is unaffected except for the total magnification. Thus h is quite unconstrained by the modeling unless restrictive assumptions are made.

Aside from the slope of the lens mass density profile, which is a global model-dependent feature, there are also local stochastic features, namely substructure. Substructure of the type that is believed to exist in and near lens galaxies, and along the lines of sight, for example, spiral arms, globular clusters, dwarf satellite galaxies, etc. can modify flux ratios of images somewhat, but will have little effect on the positions of images, and virtually no effect on the relative time delays of images. Thus our conclusions are mostly unaltered by substructure.

5. Case studies

We now show how the well-known quads illustrate the theoretical ideas of the previous sections. The systems we consider are listed in Table 1. We refer to them by the first four digits in their

names. The references to the discovery papers, observational data, and other information on these systems can be obtained from the CASTLeS Web site, maintained by Kochanek et al. (1998).

In order to illustrate the concepts developed in this paper we replace the quads with some simple models. These models are tailored to fit the image positions reasonably well but *not* to astrometric accuracy. The models are used to obtain the shape of critical and caustic curves, and the saddle point contour in the arrival time surface. The qualitative features 1–4 (cf. Section 1) are just as well reproduced by our simple models as by more sophisticated ones.

As model potential we use an elliptical isothermal with external shear

$$\psi = (a\theta_x^2 + b\theta_y^2 + 2h\theta_x\theta_y + r_c^2)^{1/2} + \gamma_1\frac{1}{2}(\theta_x^2 - \theta_y^2) + \gamma_2\theta_x\theta_y. \quad (10)$$

The core radius r_c is fixed at 0.1, while the other parameters were determined by modeling; their values are listed in Table 1. The values of the apparent shear, γ_{app} , introduced in Section 2.3 are also listed in the table.

2237, 1413, and 1411 (Figs. 6, 7, and 8 respectively) are all core quads, because their four images are approximately evenly distributed around the lens center. In the first two lenses, images 1 and 2 are almost equidistant from the center, so it is hard to distinguish them using rule (iii) of Section 3.2; but this is the only ambiguity. Note, however, that when 1 and 2 are equidistant from lens center, which one is the global minimum becomes a moot point. 1413 is one of the most symmetric of all known quads, but even in this case we can apply rule (iv) and identify the upper left image as 4. The saddle of the lemniscate, 3, is then the lower right image, by rule (i). 2237 is less symmetric; after identifying the upper left image as 4, we notice that the two lower images are the closest pair in the system, making them 2 and 3, by rule (v). Thus the upper right image is the global minimum, 1. The position of the source with respect to the lens center can be determined approximately by looking at the PA of 1. 2237 and 1413 do not have very large shears. On the other hand, 1411 appears to have a very elliptical lens, which is reflected in the large value of γ_{app} . If the source were located closer to the top of the plot, we could have had a lemniscate double rather than a limaçon double—common in cluster lenses, but not in galaxy lenses. 1411 is ideal for illustrating the effects of an elliptical lens, described in Section 3.4. The upper and lower images are visibly closer to the lens center compared to the right and left images, which indicates that the galaxy’s mass distribution is elongated along the upper-left to lower-right direction. The upper image, being closest to the center, is 4. The galaxy’s elongation is evident from the size and orientation of the diamond caustic; thus modeling confirms qualitative conclusions based on image geometry. 1 and 2 are hard to distinguish, suggesting that both minima are of nearly equal depth, though the left image is probably 1.

1115, 0414, and 1608 (Figs. 9, 10, and 11 respectively) are inclined quads. Such quads are the easiest to time order. The upper images in 1115 and 0414 and the lower image in 1608 are 1. The most identifiable feature of inclined quads is the close pair of images, 2 and 3 according to rule (v). The rest follows from rules of Section 3.2. In all three cases time ordering yields the pattern of extrema which is also revealed by the saddle point contours of Figures 9, 10, and 11.

1115, which has a source of external shear in the form of the group, demonstrates points 3 and 0 of the Introduction, that the direction of shear is robustly recovered by any modeling, while the value of h is much more model-dependent. Keeton & Kochanek (1997), using an SIS ellipsoid and a modified Hubble profiles for the galaxy mass distribution obtained best fit position angles of the group of -125° and -118° , respectively. Using a completely different type of modeling, non-parametric pixellated lens, Saha & Williams (1997) found that the source of shear is located at -130° (see their Fig. 2). This $\sim 5 - 10\%$ precision in determining PA of shear is to be contrasted with $\gtrsim 40\%$ uncertainty in the final h .

1115 has a well known ring, made up of merging images of QSO’s extended host galaxy. The faintest segment is the arc 4–1 (Impey et al. 1998), in agreement with the qualitative predictions of Section 3.5.

Comparison of 0414 and 1608 shows the effect of shear in inclined quads. While 0414’s images are approximately equidistant from center, implying small shear, 1608’s 4 is much closer to the center than the other images, indicating the presence of shear, whose axis of mass distribution is nearly horizontal. However, 1608 is more complex than that: shear arises because the galaxy-lens is a double, possibly an interacting pair, and our simple model potential does not allow for such a complicated lens. Instead, 1608 is fit by a very elliptical potential (responsible for moving 4 closer to center, and 3 further away from center) with an opposite external shear (responsible for orienting 1,3,2 images horizontally across from 4).

1608 is pushing approximations to (and sometimes beyond) their limits. For example, Witt, Mao, & Keeton (2000), assuming a relatively general parametric lens model, derive a relation between image galacto-centric radii and time delays (their Eq. [12]). Applying this to 1608’s images 2 and 3 would actually result in negative h (because image 3 is further than 2 from the lens center). Adding significant external shear (their Eq. [18]) can produce positive h , but still not realistic values.

1422 and 0911 (Figs. 12 and 13) have large external shear due to neighboring groups (Burud et al. 1998; Kundic et al. 1997) as indicated by the distances of images from lens centers. Morphology tells us that for 1422 the source is along the long axis while for 0911 source is along the short axis (see upper panels of Figs. 3 and 4). In short-axis quads, such as 0911, the direction towards 1 is a good indicator of the direction of the source away from the lens center. Image ordering is straightforward—rule (v) helps here: the closest pair is 2 and 3. 1422 and 0911 are textbook examples of the systems where external shear dominates and the source is located on the same axis as the galaxy-lens and group (1422), and on an axis perpendicular to the galaxy-group axis (0911).

The cluster-lens Cl0024+1654 is another long-axis quad.

1933 is a 10 image system; it contains a core quad, an inclined quad, and an inclined double (Fig. 14). The double-hook traced by images indicates that sources lie nearly in a line. To see this, recall that for a centrally concentrated lens, the image of a line (i.e., the solution of one Cartesian component of the lens equation) is a line with a kink or double-hook (e.g. Witt 1993). Applying

the rules of Section 3.3 to the two quads and one double of this system (see the three right-hand panels of Fig. 14) one can infer that the three sources are nearly in a straight line. Judging by their radio spectral indices and morphology, the three sources are probably the core of a radio galaxy flanked by two radio features, possibly jet components (Nair 1998).

6. Exceptional systems

The ideas we have discussed in this paper suffice to gain a good qualitative understanding of nearly all multiply-imaged QSOs. But Nature is cunning, and very occasionally a lens turns up that looks like nothing else. Such exceptions occur if the source or the lens has multiple compact components.

Multiple source components can be disentangled using spectral properties: in the case of 1933 (discussed above) the different source components have different spectral steepness in radio, and hence the ten images can be unambiguously grouped into two quads and a double.

Systems with multiple lens components are more difficult to figure out. We comment briefly on two such lenses: B1359+154, discovered and interpreted by Rusin et al. (2001), and PMN J0134-0931, discovered by Winn et al. (2002) and interpreted by Keeton & Winn (2003).

The six-image system 1359 is very nicely summarized in Fig. 6 of Rusin et al. (2001), especially panel c. From their figure, we immediately recognize the morphology of a long-axis quad, akin to 1422. We can even guess from the figure that external shear will be contributed by galaxies (roughly) to the WNW or ESE, which is consistent with the detailed results of their paper. But—and this is the unique feature—the central potential well is due not to one galaxy but to a compact group of three galaxies. Consequently, what would have been the demagnified maximum of a limaçon has been split by two internal lemniscates, yielding two new saddle points (observed) and three maxima (demagnified and unobserved).

The five-image system 0134 is even more curious. The lens evidently consists of two galaxies (possibly a merging pair) producing three saddle points and two minima. One might perhaps describe it as a distant relative of a long-axis quad, but really the morphology is completely unlike any other known object.

We look forward to more developments on 0134 and other exceptional systems that expose the limitations of our work. But meanwhile, we hope researchers will find the simple ideas of this paper helpful in understanding the remaining (vast majority of) multiply-imaged QSOs!

This has been a somewhat unusual paper and produced some lively discussion during the peer-review process. We thank the two referees and the Editor for their comments; even where we disagreed it all helped improve the paper.

A. Interactive Java applet

We have developed a Java applet to show caustics, critical curves, and saddle-point contours interactively. It is illustrated in Figure 15. The user types in parameter values for the model potential (10) in the text fields, and inputs a source position by clicking the mouse. The applet then computes and plots the invisible curves and the image positions.

The source code for this and related Java applets are available from the authors' web pages.

REFERENCES

- AbdelSalam, H.M., Saha, P. & Williams, L.L.R. 1998, MNRAS, 294, 734
- Blandford, R. D., Kochanek, C. S., Kovner, I. & Narayan, R. 1989, Sci, 245, 824
- Blandford, R.D. & Kovner, I. 1988, Phys Rev A, 38, 4028
- Blandford, R.D. & Narayan, R. 1992, ARA&A, 30, 311
- Blandford, R.D. & Narayan, R. 1986, ApJ, 310, 568
- Bourassa, R. R. & Kantowski, R. 1975, ApJ, 195, 13
- Burud, I., Courbin, F., Lidman, C., Jaunsen, A.O., Hjorth, J., Ostensen, R., Andersen, M.I., Clasen, J.W., Wucknitz, O., Meylan, G., Magain, P.; Stabell, R. & Refsdal, S. 1998, ApJ, 501, L5
- Claeskens, J.-F. & Surdej, J. 2002, A&ARev, 10, 263
- Courbin, F., Saha, P. & Schechter, P.L. 2003, in "Gravitational Lensing: an Astrophysical Tool," Lecture Notes in Physics, ed. F. Courbin and D. Minniti, Springer-Verlag, p. 1
- Fassnacht, C.D., Pearson, T.J., Readhead, A.C.S., Browne, I.W.A., Koopmans, L.V.E., Myers, S.T. & Wilkinson, P.N. 1999, ApJ, 527, 498
- Falco E.E., Gorenstein M.V. & Shapiro, I.I. 1985, ApJ, 289, L1
- Impey, C.D., Falco, E.E., Kochanek, C.S., Lehar, J., McLeod, B.A., Rix H.-W., Peng, C.Y. & Keeton, C.R. 1998, ApJ, 509, 551
- Keeton, C.R. & Kochanek, C.S. 1997, ApJ, 487, 42
- Keeton, C.R. & Winn, J.N. 2003, ApJ, in press
- Kochanek, C.S., Keeton, C.R., McLeod, B.A. 2001, ApJ, 547, 50

- Kochanek C. S., Falco E. E., Impey C., Lehar J., McLeod B., & Rix H.-W. 1998,
<http://cfa-www.harvard.edu/castles/>
- Kovner, I. 1990, ApJ, 351, 114
- Kundic, T., Hogg, D.W., Blandford, R.D., Cohen, J.G., Lubin, L.M. & Larkin, J.E. 1997, AJ, 114,
2276
- Nair, S. 1998, MNRAS, 301, 315
- Narayan, R. 1998, New Astr, 42, 73
- Narayan, R. & Grossman, S. 1989, in "Gravitational Lenses," Lecture Notes in Physics, Vol. 330,
ed. J. M. Moran, J. N. Hewitt, and K. Y. Lo, Springer-Verlag, p.31
- Nityananda, R. & Samuel, J. 1992, PhRvD, 45, 3862
- Refsdal, S. 1964, MNRAS, 128, 307
- Rusin, D. et al. 2001, ApJ, 557, 594
- Saha, P. 2000, AJ, 120, 1654
- Saha, P. & Williams, L.L.R. 1997, MNRAS 292, 148
- Saha, P. & Williams, L.L.R. 2001, AJ, 122, 585
- Schneider, P., 1985, A&A, 143, 413
- Schneider, P., Ehlers, J. & Falco, E.E. 1992, Gravitational Lenses, Springer-Verlag, Berlin
- Wambsganss, J. 1998, Living Reviews in Relativity 1, 12. [Online article]:
<http://www.livingreviews.org/Articles/Volume1/1998-12wamb/>
- Wambsganss, J. 1990, PhD Thesis, Max-Planck-Institut fur Astrophysik, Munich, Germany
- Williams, L.L.R. & Saha, P. 1995, AJ, 110, 1471
- Williams, L.L.R. & Saha, P. 2000, AJ 119, 439
- Winn, J.N., Lovell, J.E.J., Chen, H.-W., Fletcher, A.B., Hewitt, J.N., Patnaik, A.R., Schechter,
P.L. 2002, ApJ, 564, 134
- Witt, H. J. 1993, ApJ, 403, 530
- Witt, H.-W., Mao, S. & Keeton, C.S. 2000, ApJ, 544, 98
- Wucknitz, O. 2002, MNRAS, 332, 951

Table 1: Parameters in the model potential (10) and the apparent shear (defined in subsection 2.3) for some well-known systems. The ten-image system 1933 includes two quads and hence has two apparent-shear values.

system	a	b	h	γ_1	γ_2	γ_{app}
Q2237+030	0.750	0.800	0.075	-0.040	-0.020	0.070
H1413+117	0.450	0.300	0.033	-0.060	0.050	0.118
HST14113+5211	1.100	0.600	0.188	0.090	-0.030	0.263
PG1115+080	1.200	1.400	0.004	-0.010	0.080	0.138
MG0414+0534	1.500	1.400	0.251	-0.100	-0.140	0.058
B1608+656	0.800	2.050	0.369	0.240	-0.090	0.054
B1422+231	0.600	0.600	0.000	-0.040	-0.210	0.225
RXJ0911+0551	1.450	1.300	0.027	0.240	0.050	0.274
B1933+507	0.290	0.290	-0.040	-0.010	-0.050	0.158 ± 0.007

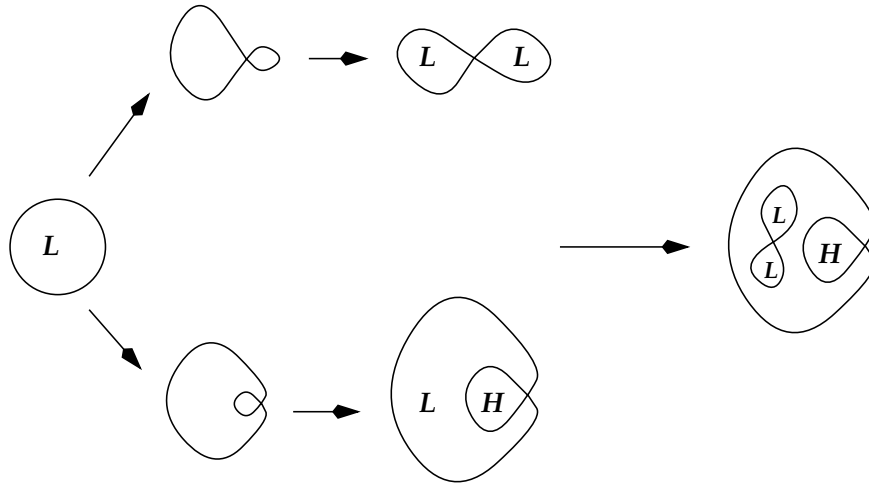


Fig. 1.— Multiple images via saddle-point contours in the arrival-time surface. Here L marks minima and H marks maxima. (Figure by H.M. AbdelSalam.)

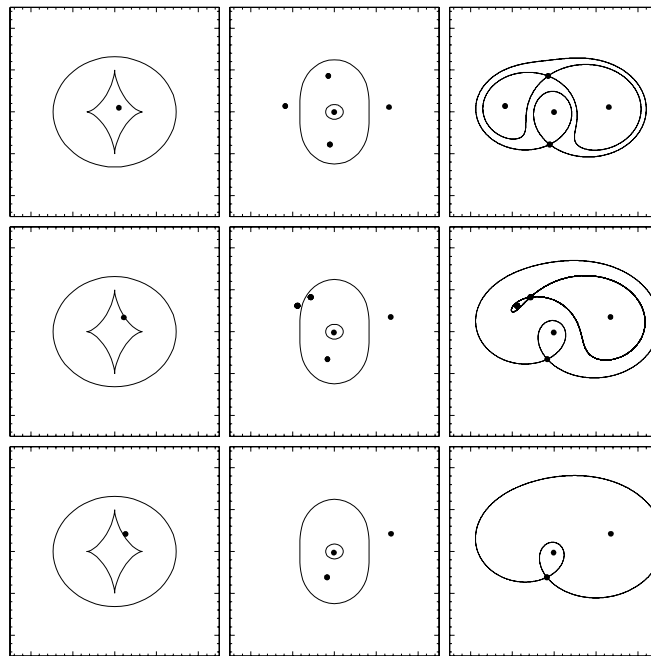


Fig. 2.— Nonsingular isothermal galaxy-lens with external shear along the vertical axis. Upper panels show a core quad, middle panels show an inclined quad, lower panels show an inclined double. Left panels show caustics in the source plane (expanded by a factor of 2) and the source, central panels show critical lines and images in the lens plane, and right panels show saddle point contours and images.

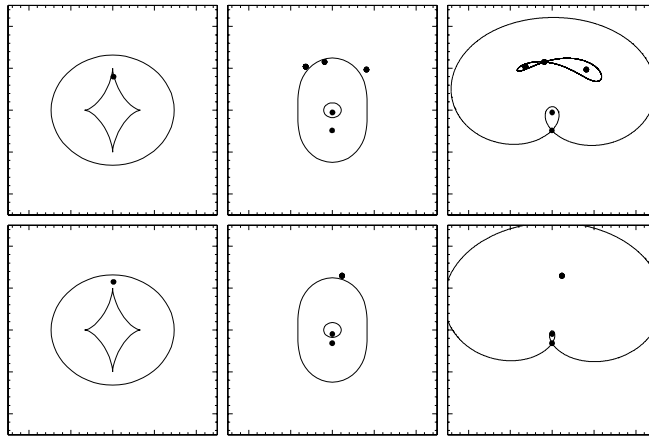


Fig. 3.— Same lens as in Figure 2. Upper panels show a long-axis quad and lower panels show an axial double, in this case a long-axis double.

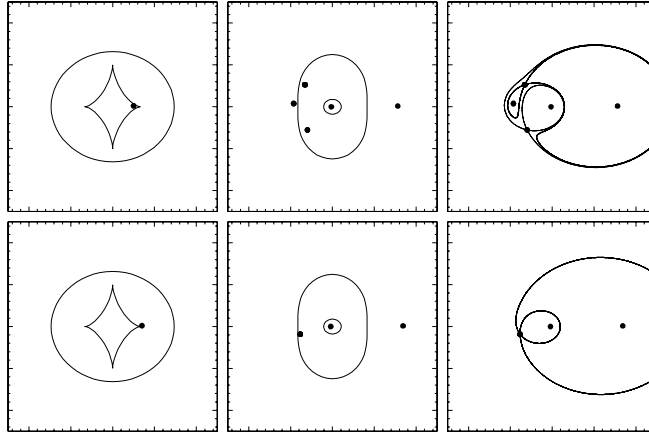


Fig. 4.— Same lens as in Figures 2 and 3. Upper panels show a short-axis quad and lower panels show an axial double, in this case a short-axis double.

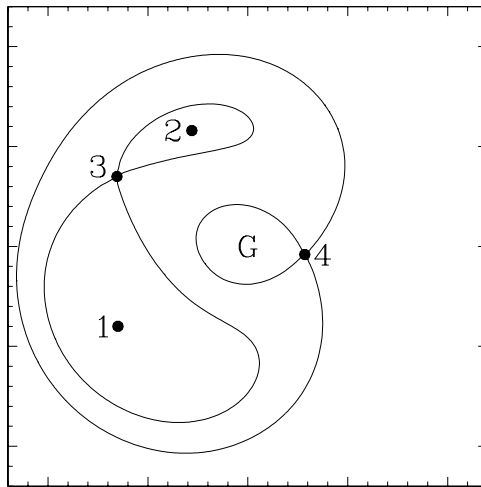


Fig. 5.— Saddle point contours in a generic quad. The images are labeled in order of their arrival times (Section 3.2); images 1 and 2 are minima, 3 and 4 are saddle points; the fifth image would be a maximum at the galaxy’s center G. In a generic double, the saddle point 3 and the minimum 2 are absent, so 4 becomes ‘2’.

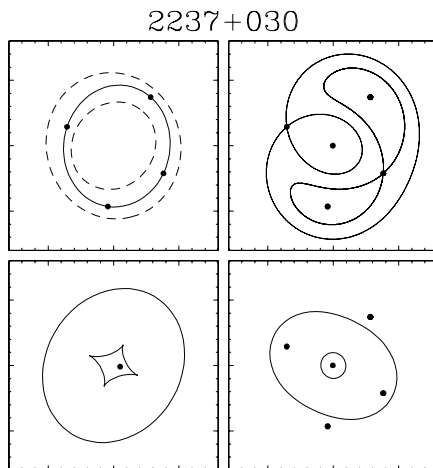


Fig. 6.— Model for 2237, a canonical core quad. Three of the panels are standard (and again the caustic panel is expanded 2-fold). In the upper-left panel, the solid curve is the apparent-shear ellipse (Section 2.3), the inner dashed ellipse shows the axes ratio of the lens potential, while the outer dashed ellipse shows the external shear. The sizes of the dashed ellipses are arbitrary, only the axis ratio and orientation is relevant. Note that the image locations are from the simple parametric model of Equation 10, and not the actual observed image positions. The differences between the two are small, and unimportant for our present purposes. 2237, and other observed quads are discussed in Section 5.

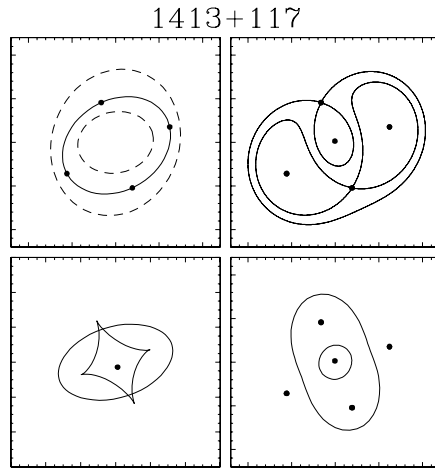


Fig. 7.— Model for 1413, another canonical core quad. Panels follow the same plan as in Figure 6.

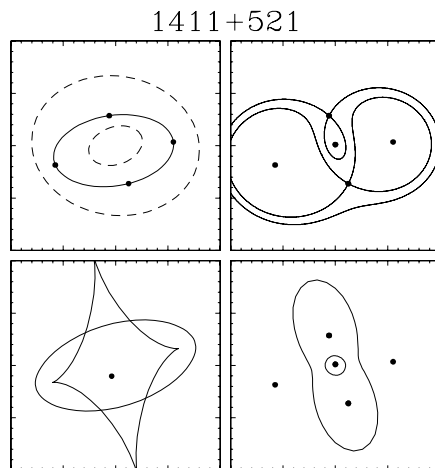


Fig. 8.— Same as Figure 6, but for 1411, a core quad.

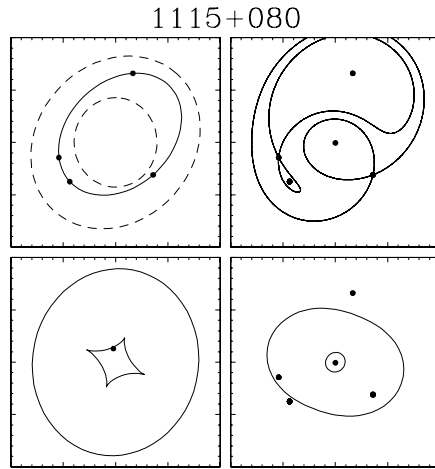


Fig. 9.— Same as Figure 6, but for 1115, an inclined quad.

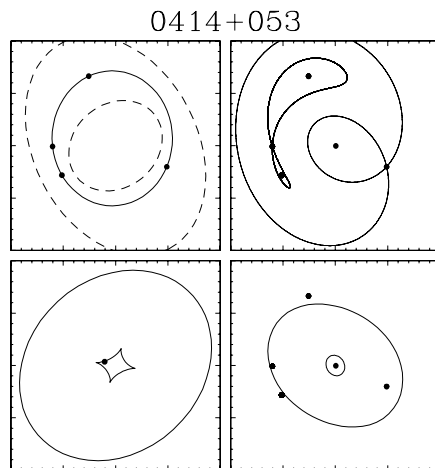


Fig. 10.— Same as Figure 6, but for 0414, an inclined quad.

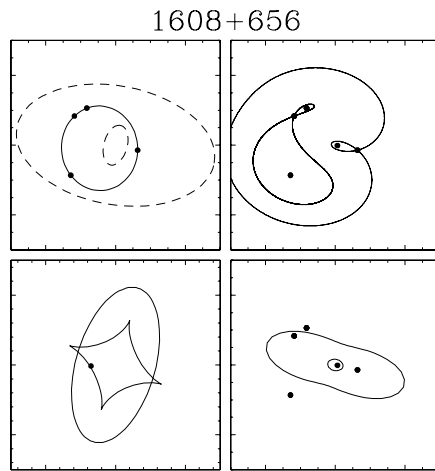


Fig. 11.— Same as Figure 6, but for 1608, an inclined quad. Because we used a simple lens potential (Equation 10), our model for 1608 is strictly speaking inaccurate, though it is still instructive—see text.

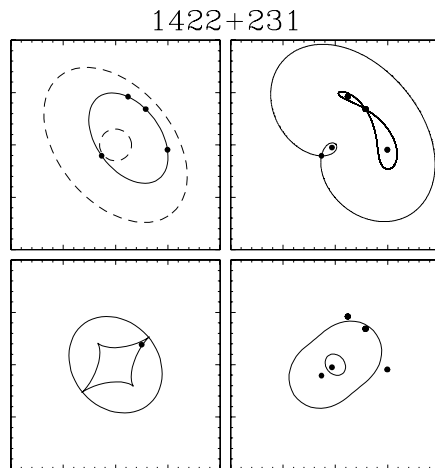


Fig. 12.— Same as Figure 6, but for 1422, a long-axis quad.

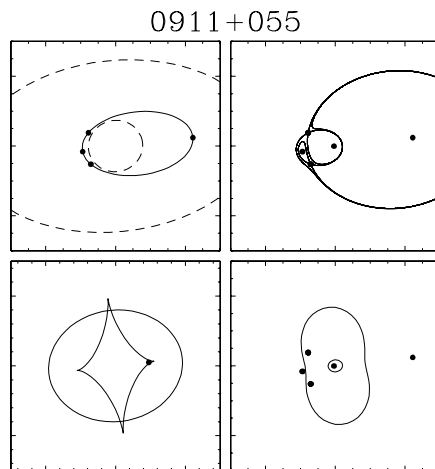


Fig. 13.— Same as Figure 6, but for 0911, a short-axis quad.

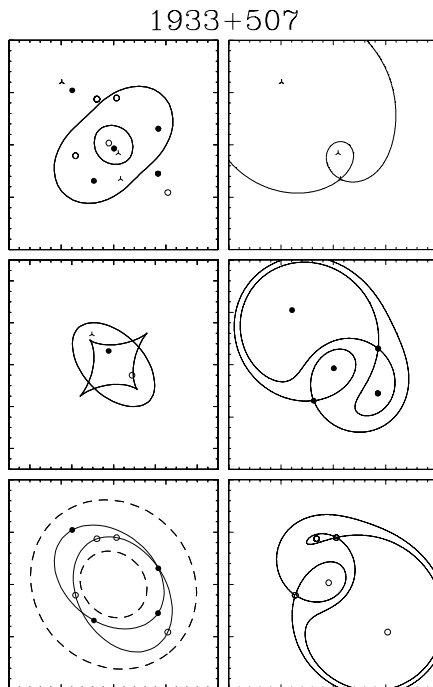


Fig. 14.— Model for 1933, a combination of three multiple-image systems; filled circles denote the images and sources of a core quad, open circles refer to an inclined quad, and skeletal stars refer to an inclined double. The right-hand panels show the arrival-time surface for each system. The upper-left panel show the critical curves and images; note the double hook traced out by the images. The middle-left panel shows caustics and source positions. The lower-left panel shows apparent-shear ellipses for both quads as solid curves. The inner dashed ellipse shows the axes ratio of the lens potential, while the outer dashed ellipse shows the external shear.

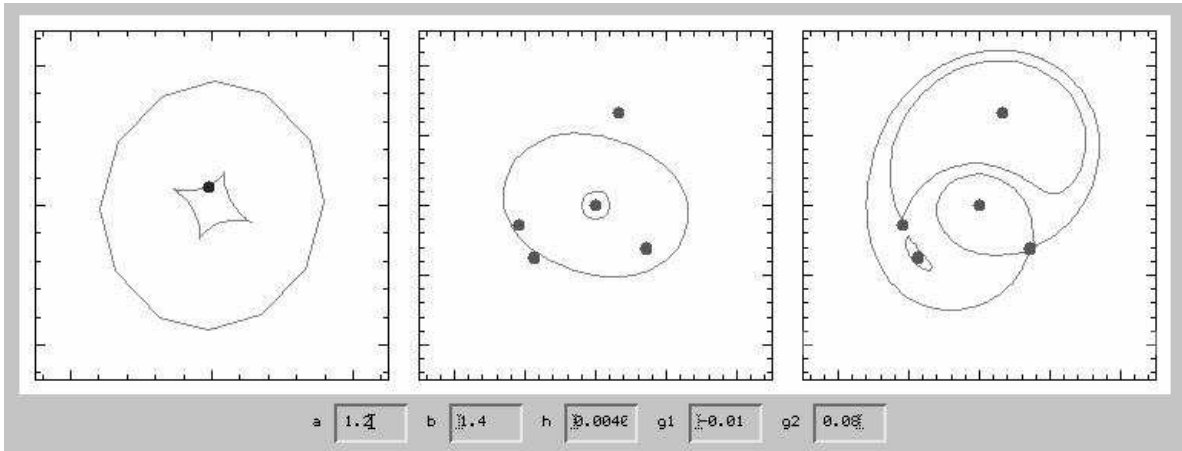


Fig. 15.— Java applet showing caustics, critical curves, and saddle-point contours. The user types in values for a , b , h , γ_1 and γ_2 (see Eq. 10) in the text field at the bottom of the applet. Source position is chosen by clicking in the left panel.